Rupture Directivity of the 2019 ML 6.3 Xiulin (Taiwan) Earthquake Estimated by Near-Field Seismograms: Implications for Source Scaling During Faulting

Ruey-Der Hwang (✉ hrd@ulive.pccu.edu.tw)
Chinese Culture University
Yi-Ling Huang
National Taiwan Ocean University
Wen-Yen Chang
National Dong Hwa University
Cai-Yi Lin
Chinese Culture University
Chiung-Yao Lin
Chinese Culture University

Research Article

Keywords: 2018 Hualien earthquake, 2019 Xiulin earthquake, Rupture directivity, Rupture velocity, Static stress drop

Posted Date: February 28th, 2023

DOI: https://doi.org/10.21203/rs.3.rs-2622549/v1

Additional Declarations:
No competing interests reported.

Tables are available in Supplementary Files section.

Rupture Directivity of the 2019 M_L 6.3 Xiulin (Taiwan) Earthquake Estimated by Near-Field Seismograms: Implications for Source Scaling During Faulting

Ruey-Der Hwang[1]*, Yi-Ling Huang[2], Wen-Yen Chang[3], Cai-Yi Lin[1], and Chiung-Yao Lin[1]

[1]Department of Geology, Chinese Culture University,
No. 55, Hwa-Kang Rd., Yang-Ming-Shan,
Taipei, 111396 Taiwan

[2]Institute of Earth Sciences, National Taiwan Ocean University,
Keelung, 202301 Taiwan

[3]Department of Natural Resources and Environmental Studies,
National Dong Hwa University,
Hualien, 974301 Taiwan

*Corresponding author: Ruey-Der Hwang
E-mail: hrd@ulive.pccu.edu.tw
Phone: 886-2-28610511
Fax: 886-2-28611801

Pure and Applied Geophysics (PAGEOPH)
Submitted on February 24, 2023

Abstract

This study deconvolved regional seismograms to derive the azimuth-dependent source time functions for the 2019 Xiulin earthquake in Hualien, Taiwan. Then, rupture directivity analysis was used to estimate the fault parameters, and the results revealed a rupture length of 11.5 km, a source duration of 7.37 s, and a rupture velocity (V_r) of 1.56 km/s, approximately 0.4 times the value of the crustal S-wave velocity. Furthermore, the multiple-event analysis indicated two subruptures during the earthquake. Notably, the average rupture and the subrupture shared the same product of $\Delta\sigma_s V_r^3$ ($\Delta\sigma_s$: static stress drop) and thus obeyed a specific source-scaling relationship. In short, the 2019 Xiulin earthquake had a relatively low V_r and a relatively high $\Delta\sigma_s$. We noted similarities between the 2018 Hualien and 2019 Xiulin earthquakes when comparing the fault parameters; rupture directivity analysis revealed that the two events occurred on a west-dipping plane with a similar strike. Therefore, the 2019 Xiulin earthquake likely constituted the remaining energy release of the 2018 Hualien earthquake.

Keywords: 2018 Hualien earthquake; 2019 Xiulin earthquake; Rupture directivity; Rupture velocity; Static stress drop.

1. Introduction

After an M_L 6.2 (M_W 6.4) earthquake struck the city of Hualien in 2018 and caused severe destruction (called the 2018 Hualien earthquake; Rau & Tseng 2019), high seismicity persisted in eastern Taiwan. Approximately 14 months later, on April 19, 2019, the Central Weather Bureau (CWB) reported an M_L 6.3 earthquake in the Xiulin region of Hualien. The 2019 event had a depth of approximately 20 km, greater than the 6.3-km depth of the 2018 event, and occurred 18 km to its southwest. The fault-plane solutions indicated that the two events both had a west-dipping plane with a strike of approximately 217° (Fig. 1). Hwang (2018) analyzed the rupture directivity of the 2018 Hualien earthquake to suggest that the west-dipping plane was the fault plane. When we superimposed the location of the 2019 Xiulin earthquake on the finite-fault model of the 2018 event (Huang & Huang 2018; Lee et al. 2019), the 2019 event appeared to occur on the 2018 event's fault plane, where it had failed to rupture. Therefore, the data indicated that the two events occurred in the same fault system. This study investigated whether the 2019 Xiulin earthquake originated from the release of the remaining energy of the 2018 Hualien earthquake.

Lee et al. (2020) derived the finite-fault model of the 2019 event and calculated a rupture velocity (V_r) of up to 4.0 km/s (i.e., a supershear rupture event) and a static stress drop ($\Delta\sigma_s$) of 3.27 MPa. These calculations differed from those of Lin et al.

(2022), who measured V_r values of 2.58 and 3.16 km/s and $\Delta\sigma_s$ values of 13.7 and 23.4 MPa for two strong motion generation areas (SGMAs). The conflicting results of the two studies imply an anticorrelation between V_r and $\Delta\sigma_s$; namely, an increase in V_r coincides with a decrease in $\Delta\sigma_s$, and vice versa. Ye et al. (2016) noted that $\Delta\sigma_s V_r^3$ remained approximately constant for a given earthquake in finite-fault inversions (Kanamori & Rivera, 2004). Hwang et al. (2020) also proposed an inverse relationship between V_r and $\Delta\sigma_s$ and further derived the product $\Delta\sigma_s V_r^3 = 29.3$ MPa·km^{3}s^{-3} from the observations of moderate-to-large earthquakes in Taiwan. Hence, we also investigated whether the 2019 Xiulin earthquake obeyed the conclusion of Hwang et al. (2020).

This study analyzed the kinematic and dynamic source parameters of the 2019 Xiulin earthquake and compared them with those of the 2018 Hualien earthquake (Huang & Huang 2018; Hwang 2018; Lee et al. 2019; Hwang et al. 2019, 2020, 2022). We first used rupture directivity analysis (e.g., Ben-Menahen 1961; Chung & Kanamori 1976; Velasco et al. 1994, 2004; Hwang et al. 2012) to investigate the kinematic source parameters, including rupture length, source duration, and V_r through the azimuth-dependent source time functions (e.g., Ammon et al. 2006; Vallée 2007; Hwang et al. 2019). In addition, we also employed multiple-event analysis to determine the dynamic source parameters, including radiated seismic energy, scaled energy, and $\Delta\sigma_s$ (Hwang et al. 2019).

2. Data

We used vertical-component acceleration seismograms from the Broadband Array in Taiwan for Seismology (BATS; IES 1996) and the CWB Geophysical Data Management System (CWB 2012) to analyze the azimuth-dependent STFs using a nonnegative time-domain deconvolution technique (Hwang et al. 2019). Only seismograms with epicentral distances of less than 50 km were analyzed to reduce the effect of structural complexity in wave propagation, where the structure can be regarded as a half-space region (Kanamori 1990). Fig. 1 illustrates the available stations around the epicenter. Before retrieving the STFs, we removed the instrument responses, converted the accelerograms into displacement, and filtered the waveforms between 0.05 and 0.33 Hz. Finally, for the follow-up deconvolution, we extracted a 35-s-long waveform, which began during the first 5 s of the P-wave arrival and ended during the last 30 s of the P-wave arrival (Figs 2 and 3).

3. Analysis and results

3.1 Source time functions (STFs)

The nonnegative time-domain deconvolution was employed to solve $g(t) *$

$s(t) = b(t)$ for retrieving the STF, with $b(t)$ as the observed waveform, $g(t)$ as the empirical Green's function (EGF), $s(t)$ as the STF, and '*' representing the convolution operator. The time domain convolution can be written in linear matrix form as $GS = B$, where G is the EGF matrix arranged according to the convolution operation, S is the STF matrix with the unknown parameters to be solved, and B is the observed waveform matrix. The damped least-squares method with nonnegative constraint (i.e., $S \geq 0$) was applied to the linear inversion (Lawson & Hanson 1974; Menke 2012) by minimising $E + \lambda^2 L$, where $E = ||B - GS||^2$, $L = ||WS||$, damping $= \lambda^2$, and W = matrix smoothness to yield the following solution:

$$S = (G^T G + \lambda^2 W^T W)^{-1} G^T B \qquad (1)$$

Details regarding the nonnegative time-domain deconvolution can be found in the work of Hwang et al. (2019). We used synthetic seismograms without source duration as the EGFs, created using the wavenumber integration technique (Herrmann 2013) in a half-space model with a P-wave velocity of 6.47 km/s, an S-wave velocity of 3.76 km/s, and a density of 2.80 g/cm^3. To generate the EGFs also needed a focal mechanism, provided by the BATS CMT (Central Moment Tensor) catalogue (IES 1996) (Fig. 1). Fig. 2 provides an example of deconvolution for station WUSB.

Fig. 3 presents the apparent STFs (aSTF) with duration variations according to the station azimuths. A relatively longer duration occurred at stations located south of the epicenter (e.g., EGC, ESL, and SHUL); by contrast, a relatively shorter duration dominated the stations situated north of the epicenter (e.g., ETLH, NACB, ENA, NNS, NNSB, and EWT). The apparent source duration variation with station azimuth formed a shape approximating a cosine or sine wave (Fig. 3), revealing unilateral rupture (Hwang 2014). This feature indicated that the 2019 Xiulin earthquake was a unilateral-faulting event with a northward rupture. We next implemented rupture directivity analysis to investigate the rupture propagation of the 2019 Xiulin earthquake.

3.2 Rupture directivity analysis

The apparent source duration (T_{ASD}) for an event with unilateral faulting (Fig. 4a) due to the rupture directivity effect can be written as follows:

$$T_{ASD} = t_0 - \frac{l}{v}\cos\delta \qquad (2)$$

where v is the wave velocity (P- or S-wave) at the source area, l is the rupture length, and t_0 is the source duration (corresponding to l/V_r) observed at the station azimuth that is perpendicular to the rupture direction. Because the STF is derived primarily from the S-wave (Fig. 2), v in Equation 2 is the S-wave velocity (3.76 km/s in this study). In Equation 2, $\cos\delta$ can be expressed below (Chung & Kanamori 1976):

$$\cos\delta = \cos i_d \cos\theta + \sin\theta \sin i_d \cos(AZ - \phi)$$

where δ is the angle between the rupture direction and a ray taking off from the hypocentre, i_d is the take-off angle of the wave ray, AZ is the station azimuth, ϕ is the horizontal rupture azimuth measured clockwise from the north, and θ is the vertical rupture angle measured upward from the vertically downward axis (see Fig. 4a). For θ larger than 90°, the event ruptures upward; for θ less than 90°, the event ruptures downward. When searching for a series of ϕ and θ, we obtained an appropriate pair of (ϕ, θ) constructing an optimal linear relationship between t_{ASD} and $\cos\delta$. Therefore, the intercept denotes the average source duration (t_0 in Equation 2), and the slope represents the propagation time ($\frac{l}{v}$ in Equation 6) used to obtain the rupture length (l) when v at the source area is known. Finally, we derived the average rupture velocity from l and t_0.

Fig. 4 shows the rupture directivity analysis of the 2019 Xiulin earthquake. The optimal pair of (ϕ, θ), identified by searching for ϕ and θ between 0° and 180° with an interval of 1°, was (5°, 76°), indicative of a slightly downward rupture along the azimuth of N5°E (Fig. 4b). The optimal linear relationship between T_{ASD} and $\cos\delta$, as illustrated in Fig. 4c, had a rupture length (l) of 11.5 km and a source duration of 7.37 s, resulting in a V_r of 1.56 km/s, about 0.4β (β is the S-wave velocity as 3.36 km/s). Unlike the results of Lee et al. (2019), which demonstrated a high V_r of 4.0 km/s for the Xiulin earthquake, the low V_r of this study is similar to the estimated V_r (1.85 km/s) of the 2018 Hualien earthquake (Hwang 2018; Hwang et al. 2020).

The angle between the optimal rupture direction and the vertically downward axis was 76°, analogous to the take-off angle (Fig. 4b). We projected the optimal rupture direction (ϕ = 5°, θ = 76°) to the focal mechanism (i.e., beachball; BATS CMT) as illustrated with a solid blue circle in Fig. 4d. The solid blue circle is closer to the red arc than the other arc; we thus verified that the west-dipping plane with a strike of 217° (from BATS CMT with the best double couple of 217°/61°/81° and 55°/30°/105°) was the fault plane (red arc) of the 2019 Xiulin earthquake.

The derived source parameters are also comparable with several empirical relationships. When using M_0 = 3 × 10^{18} Nm (Table 1), the source duration (7.37 s) from this study agrees with that (7.4 s) calculated by an empirical relationship between M_0 and T as $M_0 = 0.74 \times 10^{16} T^3$ (M_0 = seismic moment in Nm and T = source duration in s) (Hwang et al. 2020); however, the derived rupture length (11.5 km) is slightly shorter than that (14.4 km) estimated by $\log_{10} L = (1/2) \log_{10} M_0 - 8.08$ for $M_0 < 10^{20}$ Nm (L = rupture length in km; Yen & Ma 2011).

3.3 Multiple-event analysis

Because station WUSB with azimuth is approximately perpendicular to the rupture direction, we used the aSTF deconvolved from WUSB as the STF of the 2019 Xiulin earthquake (Fig. 2). Through multiple-event analysis of the STF (cf. Hwang 2013;

Hwang et al. 2019), the mainshock comprised at least three subevents, each of which had its own isosceles triangle and source duration (Table 1 and Fig. 2). Then, the seismic moment (M_0) of each subevent was calculated from the area of the isosceles triangle STF, and the radiated seismic energy (E_s) of each subevent was estimated from M_0 and its own source duration (cf. Vassiliou & Kanamori 1982). The total M_0 and E_s were 3.0×10^{18} Nm (M$_W$ 6.3) and 1.2×10^{14} Nm, respectively; these measurements were somewhat larger than those calculated by several institutes (United States Geological Survey, USGS; Global Centroid-Moment-Tensor, GCMT; BATS, and CWB) and by Lee et al. (2020). From Table 1 and Fig. 2, our results revealed that the largest subevent with M$_W$ 6.1 occurred about 3 s later than the initiation. The E_s/M_0 ratio of 3.4×10^{-5} also resembled the global average (3.0×10^{-5}; Ide & Beroza 2001) and was comparable with that of the 2018 Hualien earthquake (2.72×10^{-5}; Hwang et al. 2019). We also estimated the $\Delta\sigma_s$ of each subevent following circular cracks (Brune 1970) using $\Delta\sigma_s = \frac{7M_0}{16}\left(\frac{2\pi f_c}{2.34\beta}\right)^3$ with $f_c = \frac{2}{\pi T_{rup}}$ (Godano et al. 2015), where β is the S-wave velocity at the source area, and f_c is the corner frequency determined by the rupture time (T_{rup}), which is about 0.85 times the value of the source duration (cf. Vassiliou & Kanamori 1982; Heaton 1990). From the multiple-event analysis, the average $\Delta\sigma_s$ was measured to be 8.82 MPa using weighted M_0 (cf. Kanamori & Heaton 2000). In addition, from the E_s/M_0 ratio, the apparent stress (σ_a) was 1.35

MPa using $\sigma_a = \mu E_s/M_0$ (μ: rigidity; Wyss & Brune 1968). Because $\sigma_a/\Delta\sigma_s < 0.5$, the frictional overshoot model, in which the frictional stress is lower than the final stress on the fault plane, can be used to interpret the 2019 Xiulin earthquake rupture (Savage & Wood 1971; Zúñiga 1993; Kanamori & Rivera 2006). Table 1 lists the source parameters of the three subevents composing the 2019 Xiulin earthquake.

According to Fig. 3, the aSTF at several stations may be divided into two groups, G1 and G2. G1 consists of the first two subevents, and G2 consists of the last subevent (see Table 1). We assumed that G1 and G2 occurred along the optimal rupture direction of (5°, 76°), as measured in Fig. 4. Fig. 5a shows the rupture directivity analysis of G1 based on the optimal rupture direction of (5°, 76°) to obtain a V_r of 1.61 km/s, a rupture length of 7.26 km, and a source duration of 4.50 s. Next, subtracting the rupture length and source duration of G1 from the entire rupture length and source duration, we obtained a V_r of 1.48 km/s, a rupture length of 4.24 km, and a source duration of 2.87 s for G2 (Fig. 5b). The rupture from G1 to G2 revealed a slight deceleration.

3.4 Static stress drop

As mentioned in the preceding section, using multiple-events analysis, the average $\Delta\sigma_s$ was estimated at 8.82 MPa (Table 1). However, a standard method of calculating $\Delta\sigma_s$ is to use the rupture area (A) as: $\Delta\sigma_s = \frac{7M_0}{16}\left(\frac{\pi}{A}\right)^{3/2}$ (cf. Kanamori & Anderson, 1975). Here, we attempted to calculate the rupture area of the 2019 Xiulin earthquake by the rupture length and width. The rupture width using the aftershock distribution and the fault dip was calculated. As shown in Fig. 1, aftershocks with $M_L \geq 3.0$ appeared at depths of 18–25 km with an approximately 7-km-depth range. In addition, the focal mechanisms from GCMT, USGS, BATS, CWB, and Lee et al. (2020) indicated fault dips of 60°, 46°, 61°, 69°, and 63°, respectively. The rupture widths were then estimated to be 8.08, 9.73, 8.00, 7.50, and 7.85 km, respectively, yielding an average rupture width of 8.23 km. Hence, the rupture area is 94.65 km^2 (11.5 km × 8.23 km) for the 2019 Xiulin earthquake. Assuming a circular fault (Kanamori & Anderson 1975), through the rupture area, the 2019 Xiulin earthquake had a $\Delta\sigma_s = 7.94$ MPa, similar to the measurement (8.82 MPa) obtained through multiple-event analysis. In any case, the two results were relatively higher than that (3.27 MPa) estimated by Lee et al. (2020) but comparable with the single SMGA $\Delta\sigma_s$ of Lin et al. (2022). Through the rupture area, the average dislocation slip (D) for the 2019 Xiulon earthquake is about 0.8 m by $M_0 = \mu D A$ (Aki, 1966).

4. Discussion

The results of the rupture directivity analysis based on azimuth-dependent STFs (Figs 3 and 4) verified the fault plane to be a west-dipping plane with a strike of 217°

(BATS CMT). Such results were similar to the rupture directivity analysis of the 2018 Hualien earthquake (Hwang 2018); therefore, the two events seemingly occurred in the same fault system (Fig. 1). Furthermore, the 2018 M_W 6.4 Hualien and the 2019 M_L 6.3 Xiulin earthquakes shared additional common features. First, the two events had relatively slow average V_r values, with 1.85 km/s (0.55 β, β: S-wave velocity) for the 2018 event and 1.56 km/s (0.4 β) for the 2019 event. Second, the two earthquakes had a similar E_S/M_0, which also corresponds to the global value of 3×10^{-5} (Ide & Beroza 2001). Third, both events could be interpreted using the frictional overshoot model, i.e., the final stress on the fault plane is larger than the frictional stress (cf. Kanamori and Rivera, 2006). Fourth, even though the $\Delta\sigma_s$ of the 2019 event was larger than that of the 2018 event, the two events had a similar product $\Delta\sigma_s V_r^3$, a finding that closely agrees with the suggestion of Hwang et al. (2020), i.e., $\Delta\sigma_s V_r^3 = 29.3$ MPa·km^3/s^3 for Taiwan's moderate-to-large earthquakes (Fig. 6). Fifth, the 2019 event seemingly occurred on an unruptured area of the 2018 event's fault plane when superimposed on the finite-fault models of Huang and Huang (2018) and Lee et al. (2020). From these, a high level of similarities is evident between the 2018 and 2019 events. Hence, the 2019 event likely originated from the release of the remaining energy of the 2018 event. Table 2 lists the source parameters of the 2018 and 2019 events for comparison.

In addition, we investigated whether the subruptures during faulting corresponded to the proposed source-scaling relationship, having $\Delta\sigma_s V_r^3 = 29.3$ MPa·km³/s³ (Hwang et al. 2020). As shown in Table 1 and Fig. 5, the subrupture of G1 had a V_r of 1.61 km/s and a $\Delta\sigma_s$ of 8.11 MPa, resulting in $\Delta\sigma_s V_r^3 = 33.85$ Mpa·km³/s³; the subrupture of G2 had a V_r of 1.48 km/s and a $\Delta\sigma_s$ of 10.77 MPa, leading to $\Delta\sigma_s V_r^3 =$ 34.91 MPa·km³/s³ (Fig. 5b). Both subruptures also had the similar $\Delta\sigma_s V_r^3$ to obey the source-scaling relationship proposed by Hwang et al. (2020).

Unlike a high V_r (4.0 km/s) obtained by Lee et al. (2020) using the rupture wavefront of their finite-fault model, our study derived a relatively slow V_r (1.56 km/s). In order to investigate the validity of the derived V_r, we implemented a parameter called radiation efficiency (η_R), generally defined as $\eta_R = E_s/E_{s0} = E_s/(E_s + E_g)$, where the available energy $E_{s0} = (\frac{1}{2})\Delta\sigma_s DA$, and E_g is the fracture energy (D: dislocation slip; A: rupture area) (cf. Venkataraman & Kanamori 2004; Kanamori & Rivera 2006; Wang 2006). For subshear earthquakes with $V_r < \beta$ (β: S-wave velocity), then $\eta_R <$ 1; for supershear earthquakes with $V_r > \beta$, then η_R is possibly close to 1.0 (Kanamori 2004). For a frictional overshoot model, E_{s0} might be overestimated; then the original E_{s0} must be reduced to $0.6E_{s0}$ for $V_r = 0.9\beta$ and $0.7E_{s0}$ for $V_r = 0.6\beta$ (Madariaga 1976). In addition, η_R can also be estimated by V_r. For model III crakes, we have $\eta_R = 1 - \sqrt{(1 - V_r/\beta)/(1 + V_r/\beta)}$ in the subshear case (Husseini & Randall 1976; Husseini 1977). From E_s and $\Delta\sigma_s$ estimated in this study, we obtained

$\eta_R = 0.31$; in addition, using the derived V_r to yield $\eta_R = 0.35$. The two estimations are close to each other. Because the 2019 Xiulin earthquake rupture belongs to the frictional overshoot, the value of η_R might be increased to 0.4–0.5, comparable with the η_R of the 2018 Hualien earthquake (Hwang et al. 2022). Here, whether η_R is estimated from E_s and $\Delta\sigma_s$ or V_r, η_R is always less than 1.0. Therefore, we suggest that the 2019 Xiulin earthquake should have a slow V_r, indicating a subshear earthquake rather than a supershear one.

6. Conclusions

The rupture directivity analysis of the 2019 Xiulin earthquake from the azimuth-dependent STFs, deconvolved from regional seismograms, indicated a relatively slower rupture velocity (~0.4 times the crustal S-wave velocity) and verified a west-dipping plane to be the fault plane. Observations from the average rupture and the subrupture both obeyed the proposed source-scaling relationship (i.e., $\Delta\sigma_s V_r^3$ = constant; Hwang et al. 2020). In addition, we noted similarities in the source parameters of the 2018 Hualien and 2019 Xiulin earthquakes. Therefore, our findings indicate that the 2019 Xiulin event was likely the remaining energy of the 2018 Hualien earthquake.

Acknowledgements We first thank the Central Weather Bureau (CWB) and the

Institute of Earth Sciences(IES), Academia Sinica, Taiwan, for permitting the use of their earthquake catalog and seismograms. The National Science Council, ROC, financially supported this study under Grant No. MOST110-2116-M-034-004.

Authors' contributions

RD contributed to the conception and design of the study, conducted the analyses, and drafted the manuscript. YL contributed to the discussion and interpretation and revised the manuscript. WY contributed to the discussion and interpretation. CY and CY drew the part of the figures. All authors read and approved the final manuscript.

Competing interests

The authors declare that they have no competing interests.

Data Availability

The seismograms were acquired from the Broadband Array in Taiwan for Seismology (BATS; https://bats.earth.sinica.edu.tw) and the Central Weather Bureau Geophysical Data Management System (CWB GDMS; https://gdmsn.cwb.gov.tw). The earthquake catalog and focal mechanisms were from the CWB GDMS and BATS.

References

Aki, K. (1966). Generation and propagation of G waves from the Niigata earthquake of June 16, 1964, 2, estimation of earthquake moment, released energy, and stress-strain drop from the G wave spectrum. *Bulletin of the Earthquake Research Institute, University of Tokyo*, *44*, 73–88.

Ammon, C. J., Velasco, A. A., & Lay, T. (2006). Rapid estimation of first-order rupture characteristics for large earthquakes using surface waves: 2004 Sumatra-Andaman earthquake. *Geophysical Research Letters*, *33*, L14314, doi:10.1029/2006GL026303.

Ben-Menahem, A. (1961). Radiation of seismic surface-waves from finite moving sources. *Bulletin of the Seismological Society of America*, *51*, 401–435.

Brune, J. N. (1970). Tectonic stress and the spectra of seismic shear waves from earthquakes. *Journal of Geophysical Research*, *75*, 4997–5009.

Central Weather Bureau (CWB, Taiwan), (2012). Central Weather Bureau Seismographic Network [Data set]. International Federation of Digital Seismograph Networks. https://doi.org/10.7914/SN/T5.

Chung, W.-Y., & Kanamori, H. (1976). Source process and tectonic implications of the Spanish deep-focus earthquake of March 29, 1954. *Physics of the Earth and Planetary Interiors*, *13*, 85–96.

Godano, M., Bernard, P., & Dublanchet, P. (2015). Bayesian inversion of seismic spectral ratio for source scaling: Application to a persistent multiplet in the western Corinth rift. *Journal of Geophysical Research Solid Earth*, *120*, 7683–7712.

Heaton, T. H. (1990). Evidence for and implications of self-healing pulses of slip in earthquake rupture. *Physics of the Earth and Planetary Interiors*, *64*, 1–20.

Herrmann, R. B. (2013). Computer programs in seismology: An evolving tool for instruction and research. *Seismological Research Letters*, *84*, 1081–1088.

Huang, M.-H., & Huang, H.-H. (2018). The complexity of the 2018 Mw 6.4 Hualien earthquake in east Taiwan. *Geophysical Research Letters*, *45*, 13,249–13,257.

Husseini, M. I., & Randall, M. J. (1976). Rupture velocity and radiation efficiency. *Bulletin of the Seismological Society of America*, *66*, 117–1187.

Husseini, M. I. (1977). Energy balance for formation along a fault. *Geophysical Journal of the Royal Astronomical Society*, *49*, 699–714.

Hwang, R.-D. (2013). Multiple event analysis of the 2008 Mw 7.9 Wenchuan earthquake: Implications for variations in radiated seismic energy during faulting. *Terrestrial, Atmospheric and Oceanic Sciences*, *24*, 709–719

Hwang, R.-D. (2014). First-order rupture features of the 2011 Mw 9.0 Tohoku (Japan) earthquake from surface waves. *Journal of Asian Earth Sciences*, *81*, 20–27.

Hwang, R.-D. (2018). Source time functions of the February 6, 2018, Hualien earthquake. Academic Seminar of the 0206 Hualien Earthquake Sequence, Central Weather Bureau, Taipei City, Taiwan. (in Chinese)

Hwang, R.-D., Ho, C.-Y., Chang, W.-Y., Lin, T.-W., Huang, Y.-L., Lin, C.-Y., & Lin, C.-Y. (2020). Relationship between seismic moment and source duration for seismogenic earthquakes in Taiwan: Implications for the product of static stress drop and the cube of rupture velocity. *Pure and Applied Geophysics*, *177*, 3191–3203

Hwang, R.-D., Huang, Y.-L., Chang, W.-Y., Lin, C.-Y., Lin, C.-Y., & Chang, J.-P. (2022). Rise time of the 2018 M_W 6.4 Hualien earthquake revealed by source time functions: A restrictive estimation of static stress drop. *Physics of the Earth and Planetary Interiors*, *327*, 106878.

Hwang, R.-D., Lin, C.-Y., Lin, C.-Y., Chang, W.-Y., Lin, T.-W., Huang, Y.-L., & Chang, J.-P. (2019). Multiple-event analysis of the 2018 M_L 6.2 Hualien earthquake from source time functions. *Terrestrial, Atmospheric and Oceanic Sciences*, *30*, 367–376.

Hwang, R.-D., Lin, T.-W., Wu, C.-C., Chang, W.-Y., & Chang, J.-P. (2012). Reexamining the source parameters of the 2010 M_L 6.4 JiaSian (Taiwan) earthquake using the inversion of teleseismic *P*-waves. *Journal of Asian Earth Sciences*, *48*, 24–30.

Ide, S., & Beroza, G. C. (2001). Does apparent stress vary with earthquake size? *Geophysical Research Letters*, *28*, 3349–3352.

Institute of Earth Sciences Academia Sinica Taiwan, (1996). Broadband Array in Taiwan for Seismology. Institute of Earth Sciences, Academia Sinica, Taiwan. Other/Seismic Network. doi:10.7914/SN/TW.

Kanamori, H., & Anderson, D. L. (1975). Theoretical basis of some empirical relations in seismology. *Bulletin of the Seismological Society of America*, *65*, 1073–1095.

Kanamori, H., & Heaton, T. H. (2000). Microscopic and macroscopic physics of earthquakes. In J. B. Rundle, et al. (Eds.), Geocomplexity and the physics of earthquakes (Vol. 120, pp. 147–163). Washington: American Geophysical Monograph.

Kanamori, H., & Rivera, L. (2004). Static and dynamic scaling relations for earthquakes and their implications for rupture speed and stress drop. *Bulletin of the Seismological Society of America*, *94*, 314–319.

Kanamori, H., & Rivera, L. (2006). Energy partitioning during an earthquake. In R. E. Abercrombie et al. (Eds), Earthquakes: Radiated Energy and the Physics of Faulting (Vol. 170, pp. 3–13). Washington: American Geophysical Monograph.

Kanamori, H. (1990). Pasadena very-broad-band system and its use for real-time seismology, extended abstract for the U.S.-Japan Seminar on Earthquake

Prediction, Morro Bay, California, 12-15 September, 1988, U.S. Geological Survey open-file report, 90–98.

Kanamori, H. (2004). The diversity of the physics of earthquakes. *Proceedings of the Japan Academy Series B*, *80*, 297–316.

Lawson, C. L., & Hanson, R. J. (1974). *Solving least squares problems*, pp. 340, Prentice-Hall.

Lee, S.-J., Lin, T.-C., Liu, T.-Y., & Wong, T.-P. (2019). Fault-to-fault jumping rupture of the 2018 M_w 6.4 Hualien earthquake in eastern Taiwan. *Seismological Research Letters.*, *90*, 30–39.

Lee, S.-J., Wong, T.-P., Liu, T.-Y., Lin, T.-C., & Chen, C.-T. (2020). Strong ground motion over a large area in northern Taiwan caused by the northward rupture directivity of the 2019 Hualien earthquake. *Journal of Asian Earth Sciences*, *192*, 104095.

Lin, Y.-Y., Wen, Y.-Y., & Yen, Y.-T. (2022). Source properties of the 2019 M_L 6.3 Hualien, Taiwan, earthquake, determined by the local strong motion networks, *Geophysical Journal International*, *229*, 1665–1679.

Madariaga, R. (1976). dynamics of an expanding circular fault. *Bulletin of the Seismological Society of America*, *66*, 639–667.

Menke, W. (2012). *Geophysical Data Analysis: Discrete Inversion Theory*, pp. 293, Academic Press.

Rau, R.-J., & Tseng, T.-L. (2019). Introduction to the special issue on the 2018 Hualien, Taiwan, earthquake. *Terrestrial, Atmospheric and Oceanic Sciences*, *30*, 281–283.

Savage, J. C., & Wood, M. D. (1971). The relation between apparent stress and stress drop. *Bulletin of the Seismological Society of America*, *61*, 1381–1388.

Vallée, M. (2007). Rupture properties of the giant Sumatra earthquake imaged by empirical Green's function analysis. *Bulletin of the Seismological Society of America*, *97*, S103–S114.

Vassiliou, M. S., & Kanamori, H. (1982). The energy release in earthquakes. *Bulletin of the Seismological Society of America*, *72*, 371–387.

Velasco, A. A., Ammon, C. J., & Lay, T. (1994). Empirical Green function deconvolution of broadband surface waves: Rupture directivity of the 1992 Landers, California (Mw = 7.3), earthquake. *Bulletin of the Seismological Society of America, 84*, 735–750.

Velasco, A. A., Ammon, C. J., Farrell, J., & Pankow, K. (2004). Rupture Directivity of the November 3 2002 Denali Fault Earthquake Determined from Surface Waves. *Bulletin of the Seismological Society of America, 94*, S293–S299.

Venkataraman, A., & Kanamori, H. (2004). Observational constraints on the fracture energy of subduction zone earthquakes. *Journal of Geophysical Research*, *109*, B05302, doi:10.1029/2003JB002549.

Wang, J.-H. (2006). Energy release and heat generation during the 1999 Ms7.6 Chi-Chi, Taiwan, earthquake. *Journal of Geophysical Research*, *111*, B11312, doi:10.1029/2005JB004018.

Wyss, M., & Brune, J. N. (1968). Seismic moment, stress, and source dimensions for earthquakes in the Califorina-Nevada regions. *Journal of Geophysical Research*, *73*, 4681–4694.

Ye, L., Lay, T., Kanamori, H., & Rivera, L. (2016). Rupture characteristics of major and great ($M_w \geq 7.0$) megathrust earthquakes from 1990 to 2015: 1. Source parameter scaling relationships. *Journal of Geophysical Research Solid Earth*, 121, doi:10.1002/2015JB012426.

Yen, Y.-T., & Ma, K.-F. (2011). Source-scaling relationship for M 4.6–8.9 earthquakes, specifically for earthquakes in the collision zone of Taiwan. *Bulletin of the Seismological Society of America*, *101*, 464–481.

Zúñiga, R. F. (1993). Frictional overshoot and partial stress drop. Which one? *Bulletin of the Seismological Society of America*, *83*, 939–944.

Figure Captions

Figure 1. Locations of the 2019 Xiulin earthquake and its aftershocks in eastern Taiwan. Also included is the 2018 Hualien earthquake. The stars indicate the epicenters of the two mainshocks. The blue and red circles indicate the aftershocks within one month for the Xiulin and Hualien earthquakes, respectively. Aftershock distributions with depths are illustrated in two profiles, AA' along the strike and BB' vertical to the strike. Focal mechanisms are from the BATS CMT catalogue. The triangles represent the seismic stations used in this study.

Figure 2. Nonnegative time-domain deconvolution for station WUSB. From top to bottom, the blue and red lines denote the observed and reconstructed P-waves; the black line is the empirical Green's function (EGF), which was created from a half-space velocity model. The bottom line is the deconvolved source time function (STF), and the blue shading represents the multiple-event analysis.

Figure 3. (Left) The stations used for deconvolution. The yellow and purple triangles denote the stations from the CWB and the BATS. The star is the epicenter of the mainshock. (Middle) The source time functions (STFs) were obtained through nonnegative time-domain deconvolution. The dashed lines represent two subruptures (also see Fig. 5). (Right) Comparison of the observed (blue lines) and reconstructed (red lines) P-waves.

Figure 4. (A) A coordinate system for a source rupture in space. O is the hypocentre, R is the termination of the rupture, $\overrightarrow{OR}$ is the rupture direction, and l is the rupture length. ϕ and θ are the angles that describe the rupture in space, where ϕ is the horizontal rupture azimuth measured clockwise from the north and θ is the vertical rupture angle measured upward from the Z-axis. In addition, i_d is the take-off angle of a wave ray, AZ is the station azimuth, and δ is the angle between the rupture direction and a ray taking off from the hypocentre and controls the rupture directivity of the source. (B) Rupture directivity analysis to search for the optimal rupture azimuth (θ, ϕ), which is (5°, 76°). (C) A plot of T_{ASD} versus cosδ in accordance with the optimal rupture azimuth in (B). (D) The optimal rupture azimuth is projected on the equal-area net to indicate the fault plane (red arc) from the fault-plane solutions of the BATS CMT.

Figure 5. (A) Rupture directivity analysis for the first subrupture (G1) following the optimal rupture azimuth of (5°, 76°). Please also see Fig. 4. (B) Schematic of the subruptures G1 and G2 and their corresponding rupture parameters. The rupture length and duration of G2 were obtained by subtracting the values of G1 from the total rupture length and duration.

Figure 6. Log–log plot of rupture velocity (V_r) and static stress drop ($\Delta\sigma_s$) for Taiwan's moderate-to-large earthquakes. Excluding the squares from this study, the data

plotted are from Hwang et al. (2020). G1 and G2 represent the two subruptures of the 2019 Xiulin earthquake (also see Fig. 5).

Figures

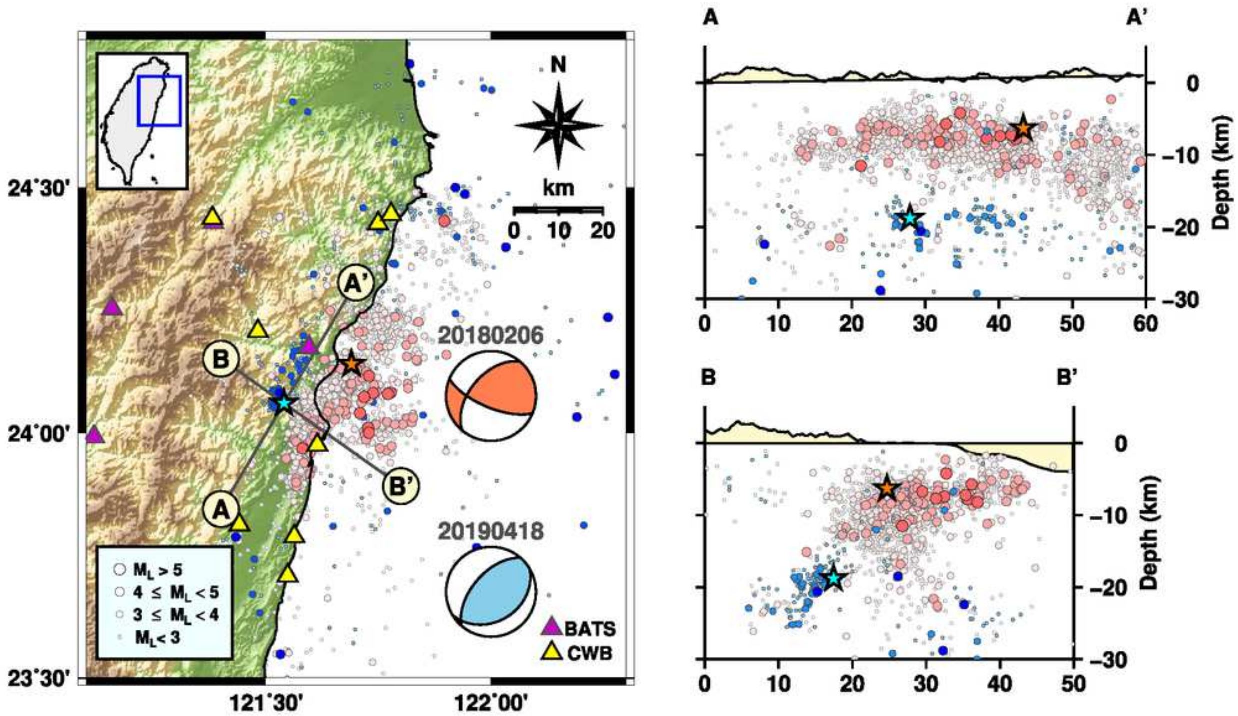

Figure 1 (Hwang et al., 2023)

Figure 1

Locations of the 2019 Xiulin earthquake and its aftershocks in eastern Taiwan. Also included is the 2018 Hualien earthquake. The stars indicate the epicenters of the two mainshocks. The blue and red circles indicate the aftershocks within one month for the Xiulin and Hualien earthquakes, respectively. Aftershock distributions with depths are illustrated in two profiles, AA’ along the strike and BB’ vertical to the strike. Focal mechanisms are from the BATS CMT catalogue. The triangles represent the seismic stations used in this study.

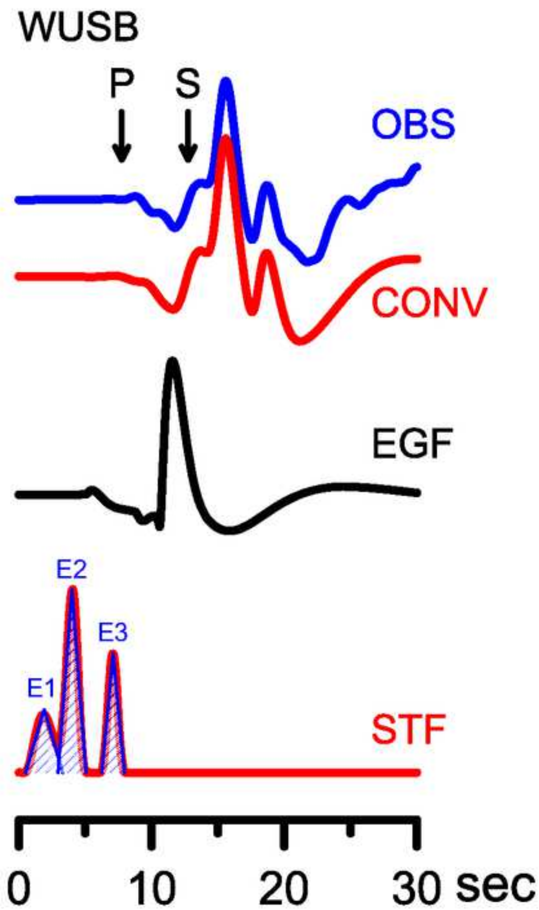

Figure 2 (Hwang et al., 2023)

Figure 2

Nonnegative time-domain deconvolution for station WUSB. From top to bottom, the blue and red lines denote the observed and reconstructed P-waves; the black line is the empirical Green's function (EGF), which was created from a half-space velocity model. The bottom line is the deconvolved source time function (STF), and the blue shading represents the multiple-event analysis.

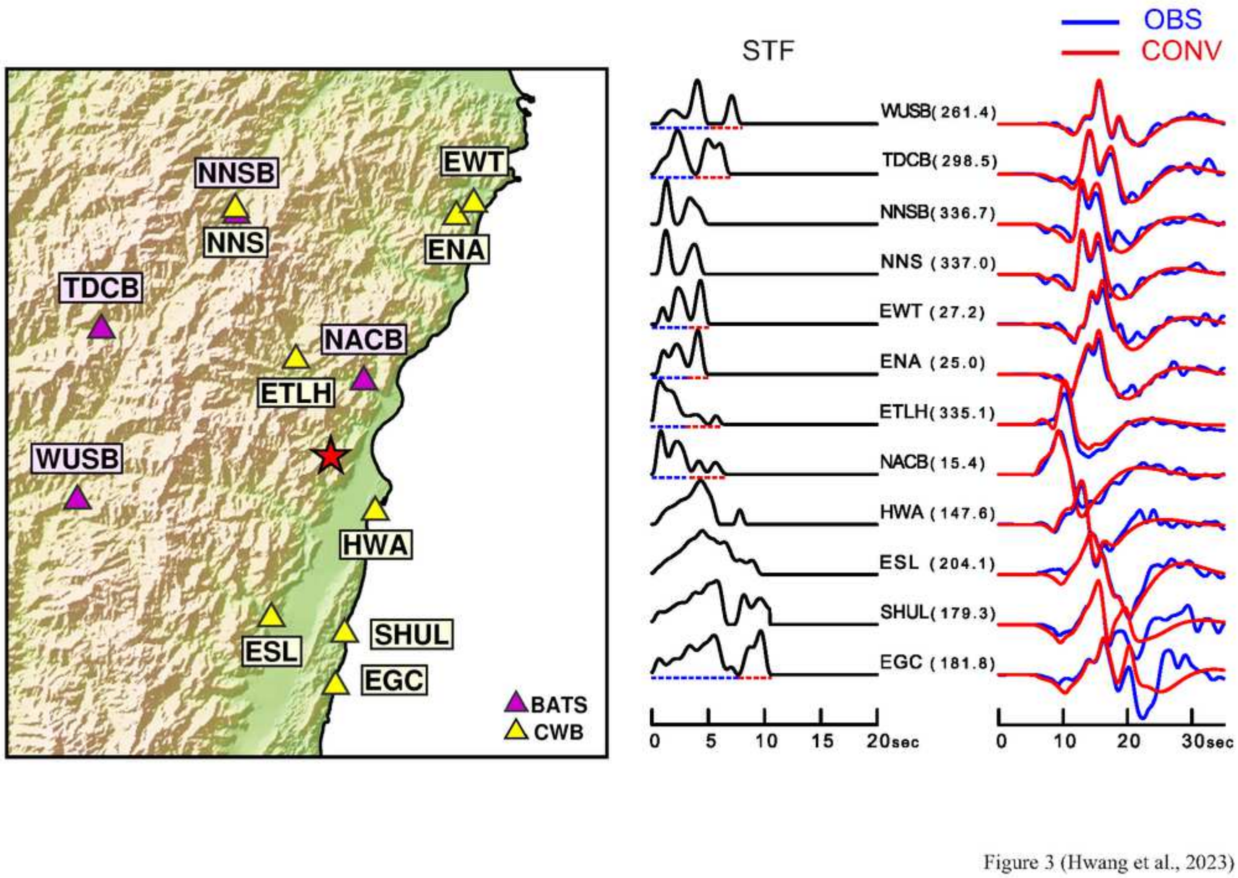

Figure 3

(Left) The stations used for deconvolution. The yellow and purple triangles denote the stations from the CWB and the BATS. The star is the epicenter of the mainshock. (Middle) The source time functions (STFs) were obtained through nonnegative time-domain deconvolution. The dashed lines represent two subruptures (also see Fig. 5). (Right) Comparison of the observed (blue lines) and reconstructed (red lines) P-waves.

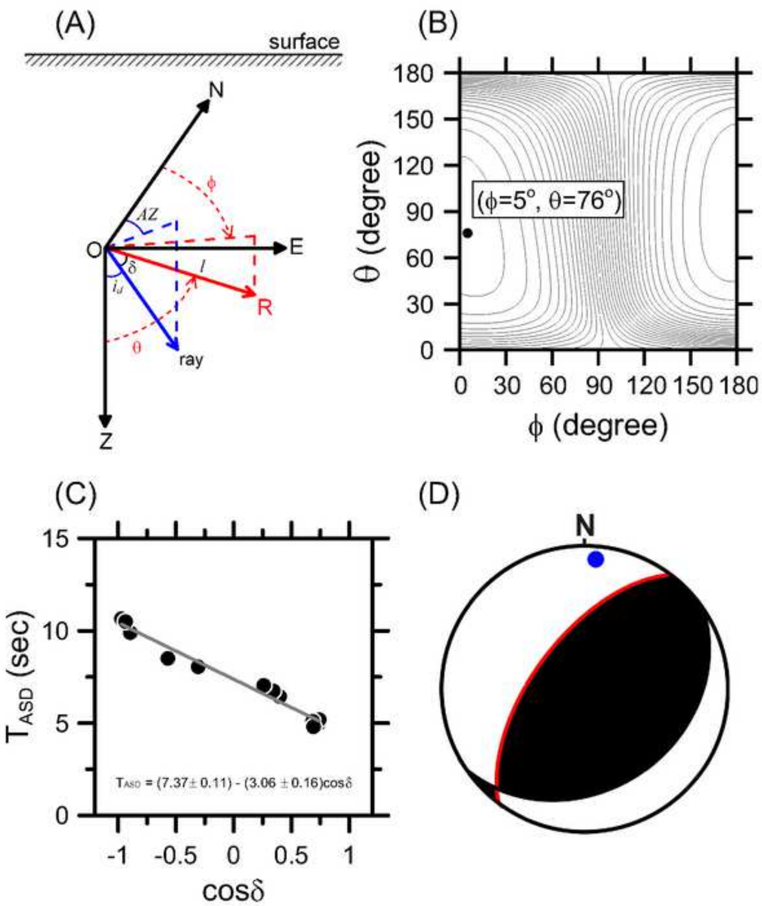

Figure 4 (Hwang et al., 2023)

Figure 4. (A) A coordinate system for a source rupture in space. O is the hypocenter, R is the termination of the rupture, $\overline{OR}$ is the rupture direction, and l is the rupture length. ϕ and θ are the angles that describe the rupture in space, where ϕ is the horizontal rupture azimuth measured clockwise from the north and θ is the vertical rupture angle measured upward from the Z-axis. In addition, i_d is the take-off angle of a wave ray, AZ is the station azimuth, and δ is the angle between the rupture direction and a ray taking off from the hypocentre and controls the rupture directivity of the source. (B) Rupture directivity analysis to search for the optimal rupture azimuth (θ, ϕ), which is (5°, 76°). (C) A plot of T_{ASD} versus cosδ in accordance with the optimal rupture azimuth in (B). (D) The optimal rupture azimuth is projected on the equal-area net to indicate the fault plane (red arc) from the fault-plane solutions of the BATS CMT.

Figure 4

See image above for figure legend

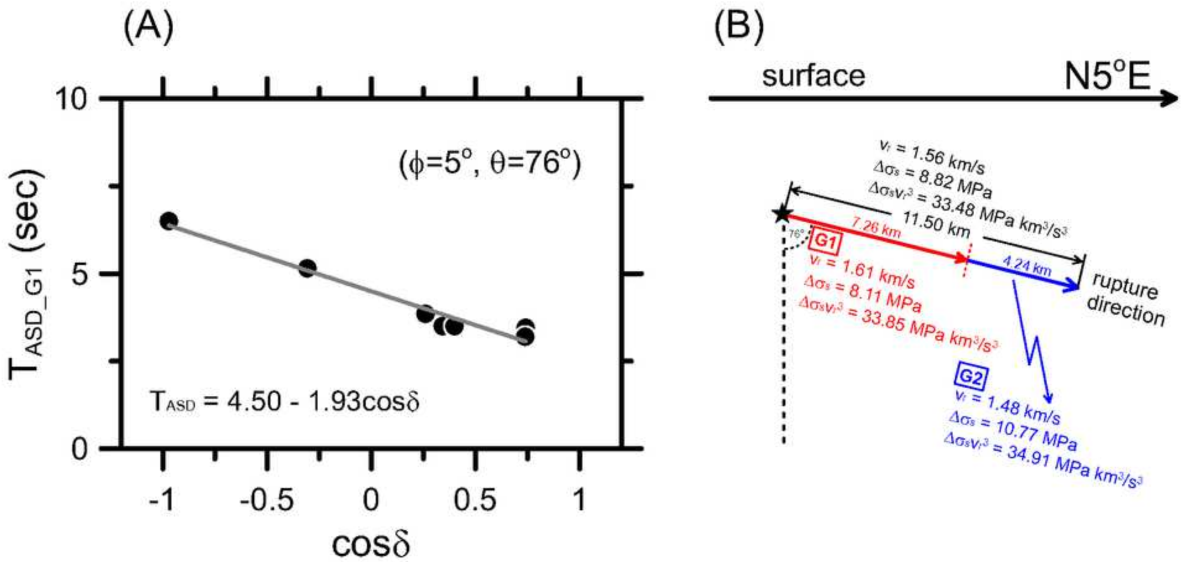

Figure 5 (Hwang et al., 2023)

Figure 5

(A) Rupture directivity analysis for the first subrupture (G1) following the optimal rupture azimuth of (5°, 76°). Please also see Fig. 4. (B) Schematic of the subruptures G1 and G2 and their corresponding rupture parameters. The rupture length and duration of G2 were obtained by subtracting the values of G1 from the total rupture length and duration.

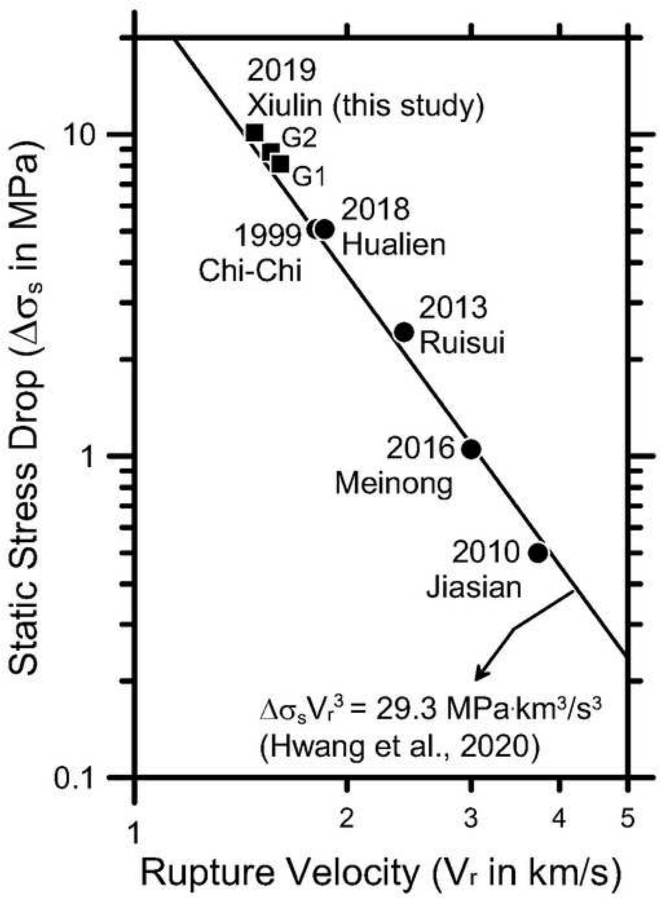

Figure 6 (Hwang et al., 2023)

Figure 6. Log–log plot of rupture velocity (V_r) and static stress drop ($\Delta\sigma_s$) for Taiwan's moderate-to-large earthquakes. Excluding the squares from this study, the data plotted are from Hwang et al. (2020). G1 and G2 represent the two subruptures of the 2019 Xiulin earthquake (also see Fig. 5).

Figure 6

See image above for figure legend

Supplementary Files

This is a list of supplementary files associated with this preprint. Click to download.

- Table12.pdf